https://doi.org/10.1016/j.addma.2023.103897

Revealing thermal behavior, cracking behavior, phase and microstructure formation of a ternary equiatomic alloy additively manufactured using directed energy deposition

S. Guan [a,*], D. Wan [b], S.H. Chen [c], L. Zhao [a], Y.L. Wang [a], B.L. Qin [a], Y.Y. Zhang [a], K.C. Chan [a,*]

[a] State Key Laboratory of Ultra-precision Machining Technology, Department of Industrial and Systems Engineering, The Hong Kong Polytechnic University, Hong Kong, China

[b] Advanced Research Institute of Multidisciplinary Sciences, Beijing Institute of Technology, Zhongguancun South Street 5, 100081 Beijing, China

[c] School of Mechanical Engineering, Hefei University of Technology, Hefei, 230009, China

* Corresponding author.

Email address: shuai.guan@connect.polyu.hk (S. Guan); kc.chan@polyu.edu.hk (K.C. Chan)

Abstract:

Additive manufacturing (AM) of multi-principal element alloys (MPEAs) have recently attracted considerable attention. However, few studies focus on the thermal behavior, cracking behavior, and microstructure tunability of AM-processed MPEAs, which can significantly affect the final performance of AM MPEA parts. In this study, a ternary equiatomic MPEA CrCoNi, with a single-phase face-centered-cubic (FCC) structure, was fabricated by the AM process via directed energy deposition (DED) at different laser scan speeds (10, 30, and 50 mm/s), and special focus was given to the thermal behavior, cracking behavior and microstructure formation. The increase in the laser scan speed from 10 to 50 mm/s causes a sharp increase in temperature gradients and cooling rates by five-fold and seventeen-fold, reaching up to 1,148 K/mm and 57,778 K/s, respectively, as in-situ measured by a high-speed and high-resolution thermal pyrometer. Furthermore, the increased laser scan speed induces the severe cracking, which propagates along high angle grain boundaries and is classified as solidification cracking based on the observed protruding dendrites from the cracked plane. Although the Scheil-Gulliver solidification predicts a very narrow critical temperature range of 16 K which is indicative of a low solidification cracking susceptibility, the high temperature gradient and the resulting high thermal stress, as evidenced from the high density of dislocations and stacking faults, are believed to trigger the severe solidification cracking of the CrCoNi MPEA deposited at a high laser scan speed of 50 mm/s. With increasing the laser scan speed, the grain structure changes from elongated grains, which are roughly oriented along the build direction, to a more heterogenous grain structure with elongated grains converging towards the centerline and equiaxed grains arranged between the columns of elongated grains. Furthermore, with increasing the laser scan speed, the cellular structures are refined down to ~ 2 μm due to the increased cooling rates. These findings not only contribute to better

understanding the thermal behavior, cracking behavior, and microstructure formation of the AM-processed MPEAs, but also pave a road for further enhancing the mechanical properties of AM parts via tuning the thermal behavior and microstructures.

Keywords: Directed energy deposition; Multi-principal element alloy; Thermal behavior; Cracking behavior; Microstructure formation

1. Introduction

Deviating from conventional alloys which have a single dominant element (e.g. Fe in steels), multi-principal element alloys (MPEAs) are a new class of alloys, comprising significant atomic fractions of several elements and giving a new and near-infinite compositional space for exploration [1, 2]. Although MPEAs often comprise several base elements in equiatomic ratios (e.g. CrMnFeCoNi [3]), this is not required, and more and more non-equiatomic MPEAs (e.g. $AlCoCrFeNi_{2.1}$ [4]) have been developed. This novel alloy design approach can achieve various microstructures, including single-phase face-centered-cubic (FCC), body-centered-cubic (BCC) or hexagonal-close-packed (HCP) structures [3, 5, 6] and complex multi-phase microstructures [7]. Several MPEA systems have been designed with exceptional properties, such as high damage tolerance of CrCoNi [8] and excellent strength-ductility balance of $Al_{0.5}Cr_{0.9}FeNi_{2.5}V_{0.2}$ [7]. Hence, MPEAs have generated considerable interest in the field of metallic materials since their first emergence in 2004.

Until now, however, MPEAs are often processed by casting [9-12], powder metallurgy [13] and magnetron co-sputtering [14], etc. The conventional metallurgical processes often generate simple geometry parts, with post tooling required. For magnetron co-sputtering, it is only applicable to manufacture thin films for ultra-small-dimension devices [14]. In contrast, additive manufacturing (AM) is a process by which 3D objects are created layer upon layer from 3D models. The AM process can build industrial-scale parts with complex geometries and internal features, requiring little or no post tooling. Furthermore, the AM process is characterized by a highly localized melting and solidification process, and provides the possibility of achieving hierarchical microstructures with enhanced mechanical properties [15]. These advantages are the key drivers for the possible application of the AM process in the manufacturing of MPEAs.

Some MPEAs, with exceptional properties, have been manufactured using various AM processes in recent years, and these include CrCoNi [16-19], CrMnFeCoNi [20-29], $Al_xCoCrFeNi$ [30-38], $Co_{0.5}CrCu_{0.5}FeNi_{1.5}AlTi_{0.4}$ [39], TiZrNbMoV [40], $Co_{1.5}CrFeNi_{1.5}Ti_{0.5}Mo_{0.1}$ [41], $AlCoCrFeNiTi_{0.5}$ [42], compositionally graded MPEAs [43-45] and laminated MPEAs [46], etc. There has been indirect evidence regarding the tunable microstructures of the AM-processed MPEAs through comparing the publications by different authors. For example, in Ref. [22], a columnar grained microstructure with alternating sequence of <100> and <110> crystallographic orientations was achieved in the AM-processed CrMnFeCoNi MPEA. In contrast, it was demonstrated in Ref. [20] that a columnar grained microstructure with an obvious <100> crystallographic orientation was achieved in the AM-processed CrMnFeCoNi

MPEA. Furthermore, there have also been some reports demonstrating more random textures [27] and even some equiaxed grains [24] developed in the AM-processed CrMnFeCoNi MPEA. Owing to the diverse microstructures of the AM-processed CrMnFeCoNi MPEA, the tensile properties reported in open publications are very scattered, with yield strengths ranging from 200 – 600 MPa and tensile ductility ranging from 20% – 60% [23-28]. These results published by different authors indicate that the microstructural features of the AM-processed MPEAs, such as grain structures (columnar, equiaxed, or mixed) and grain sizes (a few micrometers to several hundred micrometers in width), are tunable, but sparse systematic studies have been reported. Furthermore, it's worth noting that, as the most critical defect, the cracks should be strictly avoided in the AM-processed parts. However, the study on the cracking behavior of the AM-processed MPEAs is very lacking. Nevertheless, in Ref. [36], the CoCrFeNi MPEA was found to be very prone to solidification cracking during the AM process, which was attributed to the large residual stress resulting from the large grain size (~ 200 μm in width, ~ 3 mm in length). Another research by Bi et al. found that the intergranular hot cracks of AM-processed CrCoNi MPEA are closely related to the high oxygen content which originates from the starting powders as well as the AM process [16]. Other cracking mechanisms, e.g. liquation cracking [47-50], strain-age cracking [51] and ductility-dip cracking [52], may be also activated in the AM process and have been reported for the conventional alloys processed by the AM process.

This study aims to reveal the microstructural formation mechanism and to probe into the cracking behavior of a ternary equiatomic MPEA CrCoNi during the directed energy deposition (DED) process which is a typical laser powder-blown AM process. The CrCoNi alloy is a single-phase FCC-structured MPEA with exceptional cryogenic fracture toughness [11, 53], which makes some complicated effects eliminated, such as liquation of some low-melting temperature phases, and hence simplifies the complexity of the study. By changing the laser scan speed and with the aid of the powerful temperature measurement technique as well as detailed microstructural characterization, we not only reveal the microstructural formation mechanism but also identify some common features that help probe into the origin of cracking. This work paves a road for tuning the microstructure and suppressing the cracking behavior of the AM-processed MPEAs, which may further enhance their properties.

2. Experimental

2.1. Starting powder

The CrCoNi pre-alloyed powder particles were manufactured by the plasma rotating electrode process (PREP). It was observed in a field emission gun scanning electron microscope (FEG-SEM) that the as-manufactured powder particles are perfectly spherical, without any satellites, indicating good flowability (Fig. 1 a). The surfaces of the particles are very clean, indicating no oxidation (Fig. 1 a). Furthermore, the dendrite morphology was also clearly observed in the magnified SEM image (Fig. 1 b). Based on SEM images, the particle diameter distribution was determined using Nano Measurer software and is shown in Fig. 1 c. It can be seen that the particle diameter is Gaussian distributed, with an average value of ~ 75 μm. Such powder particles are in

fairly good agreement with the particle size range specified by the DED system. Furthermore, very sparse spherical gas pores were occasionally observed in the sectioned particles (Fig. 1 d). This suggests a good particle quality because the gas pores in the particles may be entrapped in the final AM parts [54].

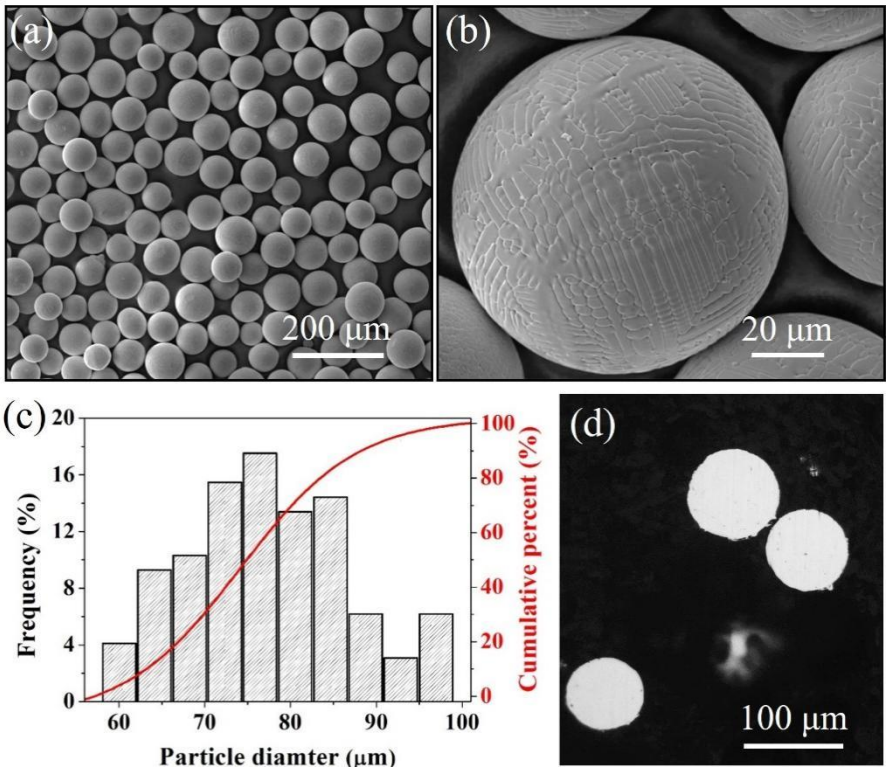

Fig. 1. (a) and (b) SEM images showing the as-manufactured CrCoNi powder particles at different magnifications. (c) Particle diameter distribution. (d) Sectioned particles showing very sparse entrapped gas pores.

2.2. Manufacturing of specimens using the DED process

The above-mentioned powder particles were loaded into a commercial DED system (LENS^{TM} MR-7), which is equipped with a 500 W IPG fiber laser with a spot size of 0.6 mm. Cuboidal specimens with dimensions of 8 mm × 8 mm × 8 mm were manufactured. During the manufacturing process, the particles were blown into the laser-created melt pool with the aid of argon gas. Each layer was scanned in a zigzag (bidirectional) way. After one layer was deposited, the deposition head was moved upwards to scan the next layer and the laser scan direction was rotated by 90° (cross-hatched). The bidirectional and cross-hatched scan strategy is schematically shown in Fig. 2. It is worth mentioning that the DED process was performed in an ultra-high-purity argon-filled chamber which is connected to an oxygen and moisture getter. This getter can absorb the trace oxygen and return cleaner argon gas to the chamber, with oxygen levels maintained below 10 ppm to minimize any potential oxidation. Furthermore, during the fabrication of these cuboidal specimens, the melt pool was continuously monitored by the ThermaViz system which incorporates a two-wavelength imaging pyrometer as well as an image acquisition and analysis software. The imaging pyrometer was placed above the LENS^{TM} MR-7 system and mounted on-axis with the laser path. A macro lens and broad band pass filter were used in the image path. The pyrometer, lens, and filter were calibrated with a tungsten strip lamp before use. The two-wavelength imaging pyrometer measures in two spectral ranges

simultaneously, and determines the temperature by comparing the radiation ratio. This imaging pyrometer could provide real-time (25 frames/s) and high resolution (12.1 μm/pixel) temperature measurements within a wide range of temperatures from 1273 to 3073 K. The measured temperature enables us to estimate the temperature gradient and cooling rate in the melt pool. The laser scan speed V_b (10, 30 and 50 mm/s) was varied to study its effects, and the corresponding specimens were designated as V_{10}, V_{30} and V_{50} specimens. Other DED process parameters, including the deposition head increment *t*, hatch spacing *h*, laser power *P*, and powder feed rate *f*, were kept constant for these cuboidal specimens, which have been optimized previously [55] and are as summarized in Table 1.

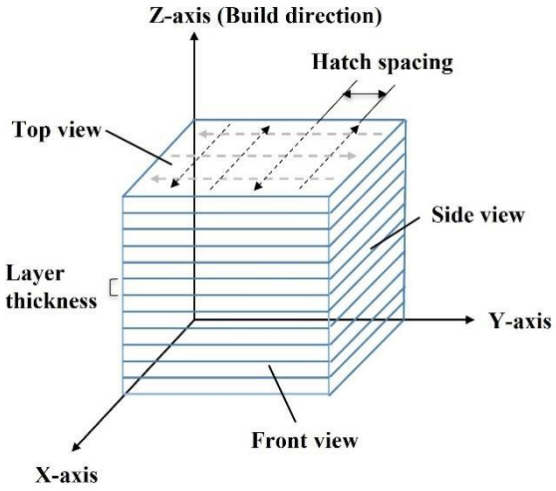

Fig. 2. Schematic of the cuboidal specimen manufactured by the DED System. The coordinate system (i.e. X-, Y-, and Z-axis), and the three cross-sections (i.e. top, front and side views) are indicated. The black and gray broken arrows represent the laser scan directions for two consecutive layers, showing the bidirectional and cross-hatched scan strategy used in this study. Furthermore, the layer thickness and the hatch spacing are also schematically shown.

Table 1

The DED process parameters used in this study.

Processing parameters	Values (units)
Deposition head increment (*t*)	102 (μm)
Hatch spacing (*h*)	457 (μm)
Laser power (*P*)	400 (W)
Laser scan speed (V_b)	10, 30 and 50 (mm/s)
Powder feed rate (*f*)	2.4 (g/min)
Scan strategy	Bidirectional and cross hatched

2.3. Material characterization and thermodynamic calculations

The oxygen levels in the starting powders and the DED-processed specimens were measured by Horiba EMGA-930 analyzer. In order to study the pores and the cracks,

the DED-processed cuboidal specimens were cut along the YZ-plane, ground, polished and then examined by a Leica optical microscope (OM). For determination of the phase formation, the X-ray diffraction (XRD) measurement was performed on Rigaku SmartLab, with the aid of the Cu Kα radiation and at a scan rate of 5 degrees per minute. The electron backscatter diffraction (EBSD) measurement was performed on the polished YZ-plane, with an acceleration voltage of 20 kV and a step size of 2 µm. EBSD data was analyzed with Orientation Imaging Microscopy (OIM) analysis software. We used neighboring confidence index (CI) correction and restricted cleanup to points with CIs less than 0.1. The FEG-SEM was used again to examine the microstructural features, e.g. melt pool boundaries, grain boundaries and solidification substructures. In order to visualize these microstructural features, the specimens were polished and electrolytically etched in a solution of 10 mL HNO_3 + 5 mL $C_2H_4O_2$ +85 mL H_2O. To reveal the crystallographic defects (e.g. dislocations, stacking faults, etc.), the DED-processed specimens were characterized by the electron channeling contrast imaging (ECCI) technique, which was carried out at an acceleration voltage of 30 kV. Furthermore, the solidification behavior of the CrCoNi MPEA was simulated by the CALculation of PHAse Diagram (CALPHAD) method, on the platform of Thermo-Calc software (v. 2019a) equipped with a high entropy alloy thermodynamic database (TCHEA v. 2.1.1).

3. Results and discussion

3.1. Thermal behavior

The imaging pyrometer on our DED system in-situ measures the temperature in the vicinity of the melt pool and can show the temperature distribution by a two-dimensional color-coded thermal image. Fig. 3 a shows a typical thermal image of the CrCoNi alloy deposited at a laser scan speed of 10 mm/s. The temperature is shown down to the liquidus temperature (i.e., 1713 K) of the investigated alloy. Therefore, the image contour is corresponding to the liquidus isotherm and hence the melt pool boundary. The whole melt pool can be roughly divided into two halves by the melt pool center (approximately the hottest point with the peak temperature). For the present case, the left half of the melt pool is experiencing heating and the right half of the melt pool is experiencing cooling. In this study, we focus more on the tail of the melt pool, which not only cools but also solidifies. In order to determine the temperature gradient and the cooling rate at the tail of the melt pool, the temperature profile corresponding to the cooling half is extracted from the thermal image along the laser scan direction (Fig. 3 a, white line). The temperature gradient curve was achieved by differentiating the temperature with the distance, and the cooling rate curve was achieved by multiplying the temperature gradient and the laser scan speed. Temperature gradient and cooling rate curves are shown in Figs. 3 b and c, respectively. Both temperature gradients and cooling rates vary within the melt pool, and herein we focus on the tail of the melt pool where solidification is occurring.

Calculations of the temperature gradient and cooling rate were also performed for V_{30} and V_{50} specimens, and the effect of the laser scan speed on the temperature gradient and cooling rate is summarized in Fig. 3 d. Obviously, the increase of the laser scan speed leads to the simultaneous increase of the temperature gradient and the cooling

rate. For example, the temperature gradient and cooling rate values for the V_{10} specimen were estimated to be 250 K/mm and 3,333 K/s, respectively, whereas both values for the V_{50} specimen were estimated to be as high as 1,148 K/mm and 57,778 K/s, respectively.

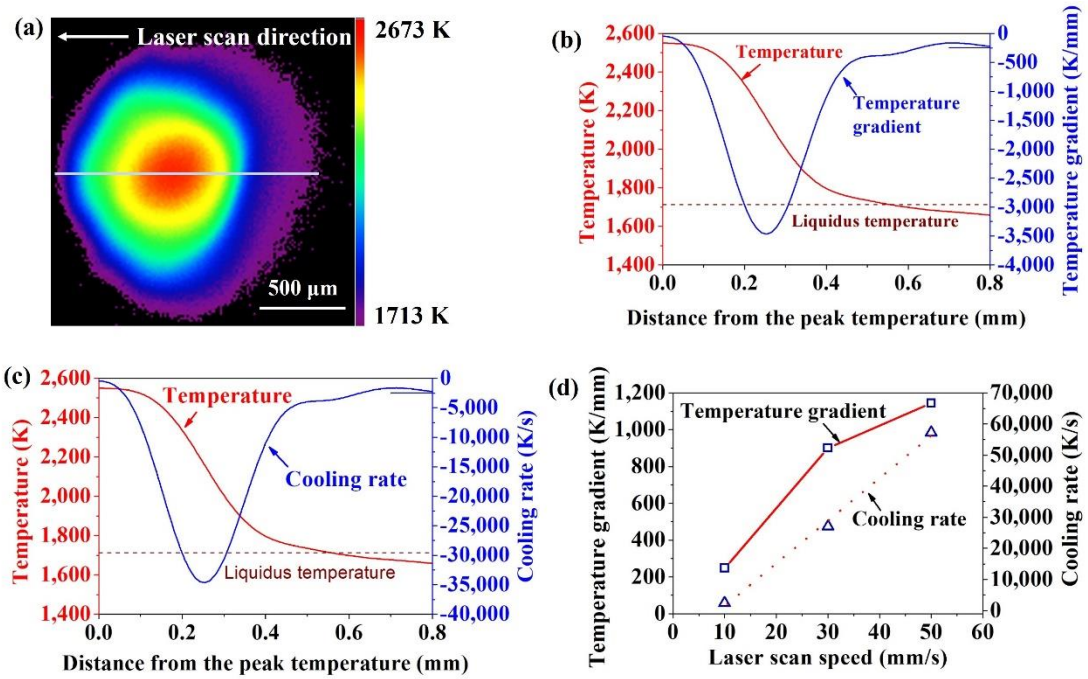

Fig. 3. (a) A typical thermal image of the V_{10} specimen. (b) Temperature profile and temperature gradient profile of the V_{10} specimen. (c) Temperature profile and cooling rate profile of the V_{10} specimen. (d) Effects of the laser scan speed on the temperature gradient and cooling rate.

3.2. Cracking behavior

3.2.1. Cracking characteristics

The OM images of the DED-processed CrCoNi specimens deposited at various laser scan speeds V_b are shown in Fig. 4. It can be seen from these micrographs that spherical pores are formed occasionally. The observed spherical pores in this study are not lack-of-fusion defects that were reported to be several hundred micrometers large, irregular and site-specific (i.e. at inter-track and inter-layer locations) [56, 57]. In this study, these spherical pores are believed to be gas pores in nature. On the one hand, the gas pores may originate from the sparse gas bubbles in the starting powders (Fig. 1 d). On the other hand, these gas pores may originate from the occasional vaporization of surface materials followed by the formation and collapse of cavities [58]. Specifically speaking, when the laser power density is enough, the metal vaporization will be activated. As a direct result, a vapor cavity would form, which facilitates the laser absorption and consequently enables the laser beam to drill to a deeper depth. Occasional collapse of these deep cavities would leave gas pores inside the melt pool.

As compared to the gas porosity, the cracks are more deleterious defects in this study

that may run several hundred micrometers and deserve more attention. To be more specific, the V_{10} specimen is free of any cracks, and in contrast, in the V_{30} specimen a few cracks are occasionally formed. As for the V_{50} specimen, the cracking phenomenon is much more pronounced.

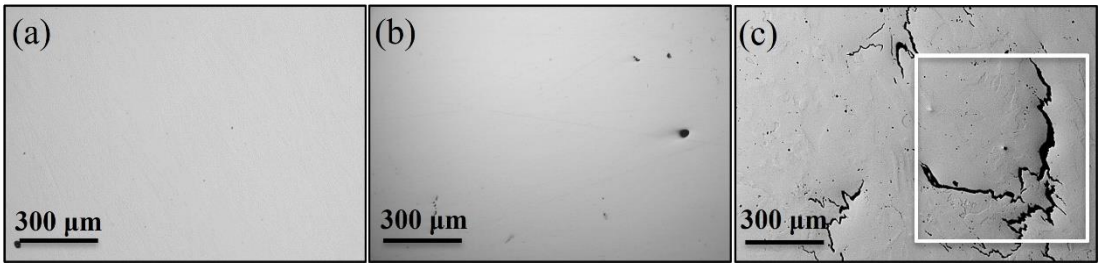

Fig. 4. Optical micrographs of the DED-processed CrCoNi specimens deposited at a laser scan speed of (a) l0, (b) 30, and (c) 50 mm/s. The rectangular region in (c) were mapped by EBSD, as shown in Fig. 5.

Unlike the cracks running along the build direction observed in the AM-ed CoCrFeNi MPEA [36], the cracks in the DED-processed CrCoNi MPEA are very random and run several hundred micrometers in various directions. To better understand the cracking behavior, the cracked region (the rectangular region in Fig. 4 c) of the V_{50} specimen was examined by EBSD with a scan area of 600 × 600 μm^2, and the result is shown in Fig. 5. It can be seen from the EBSD inverse pole figure (IPF) map that the cracks propagate along the high angle grain boundaries (HAGBs, >15°, in black) (Fig. 5 a), i.e. these cracks are intergranular cracks. In contrast, the low angle grain boundaries (LAGBs, 2° – 15°, in blue) and the subgrain interior remain uncracked. Such a phenomenon clearly suggests that the HAGBs are more sensitive to cracking. Regarding the random running directions of these intergranular cracks, it is due to the heterogeneous grain structures developed in the V_{50} specimen, i.e. the grains grow in various directions and so do the cracks. In the vicinity of the cracks, large plastic deformations were detected, as evidenced by a larger local misorientation value in the EBSD kernel average misorientation (KAM) map (Fig. 5 b).

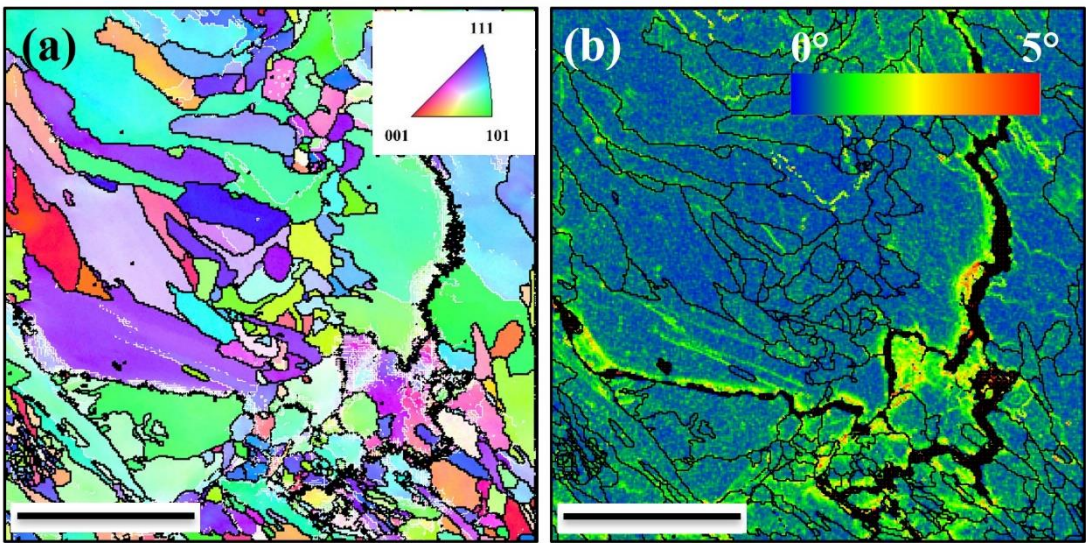

Fig. 5. EBSD (a) IPF map and (b) KAM map of a cracked region in the V_{50} specimen The HAGBs are highlighted in black in both maps. The LAGBs are highlighted in white in the IPF map. The Z-axis (i.e. the build direction) is vertically upwards, and the Y direction is horizontal. The reference axis for the IPF map is the build direction. All the scale bars are 200 μm.

3.2.2. Cracking mechanism

Several cracking mechanisms have been reported in the welding and AM literature, e.g. solidification cracking [59, 60], liquation cracking [50, 61, 62], ductility-dip cracking [63] and strain-age cracking [51]. Solidification cracking, also known as hot tearing, occurs in the mushy zone of the melt pool at the very last stage of solidification when the dendrites have coalesced and the inter-dendritic melt could initiate a crack under thermal stress [59, 60]. In contrast, liquation cracking occurs in the heat affected zone, and such cracks typically originate from the liquation of certain low melting temperature phases (e.g. eutectics and carbides) at the grain boundaries [50, 61, 62]. Obviously, these two cracking phenomenon occur in the presence of a liquid film. In contrast, ductility-dip cracking and strain-age cracking occur at a fully solid state although these two cracking mechanisms are triggered during different processes. As its name suggests, ductility-dip cracking originates from a significantly reduced ductility that often occurs in an intermediate temperature range [63]. Such a cracking behavior was well documented in Ni-based superalloys when cooled down from high temperatures after laser processing. It is worth mentioning that post ageing heat treatment is occasionally needed, and this leads to precipitation phenomenon. Although precipitation strengthens the alloys, it normally leads to the decrease in ductility and the increase in stress. Such a combined effect may also cause the cracking phenomenon, i.e. strain-age cracking [51].

To probe into the cracking origin of the V_{50} specimen in this study, the cracked region of the V_{50} specimen was examined and is shown in Fig. 6. Severe deformation was observed in the vicinity of the cracks, indicating a large thermal stress and hence a high strain level (Fig. 6 a). Furthermore, the cracks are very jagged (Fig. 6 a and b), and a high magnification SEM micrograph in Fig. 6 c shows that the cracked surface exhibits obvious protruding dendritic structures. These microstructural features lead to a judgement that these intergranular cracks are formed in the presence of a liquid film [64]. In other words, it is only when cracking occurs in the presence of a liquid film that these solidification substructures are retained on the cracked surface. Hence, the two solid-state cracking behaviors, i.e. ductility-dip cracking and strain-age cracking, could be safely excluded for the present case. As discussed before, the liquation cracking often occurs in the presence of the liquid film that originates from the liquation of some low melting point phases at grain boundaries. For example, the IN738 (or IN738LC) superalloy was reported to form multiple phases at the grain boundaries, e.g. MC-type carbides, γ-γ′ eutectics, M_3B_2 borides and Ni_7Zr_2 zirconium compounds, and the liquation of these phases were found to be the origin of micro-fissuring in the heat affected zone [50, 61, 62]. However, the CrCoNi MPEA is a typical single-phase FCC alloy, which has been well documented in Refs. [53]. The single-phase FCC structure can be also seen from our XRD patterns which will be presented later in Fig. 8. Therefore, the liquation cracking can also be excluded. These observations and discussions finally lead us to point to the solidification cracking mechanism.

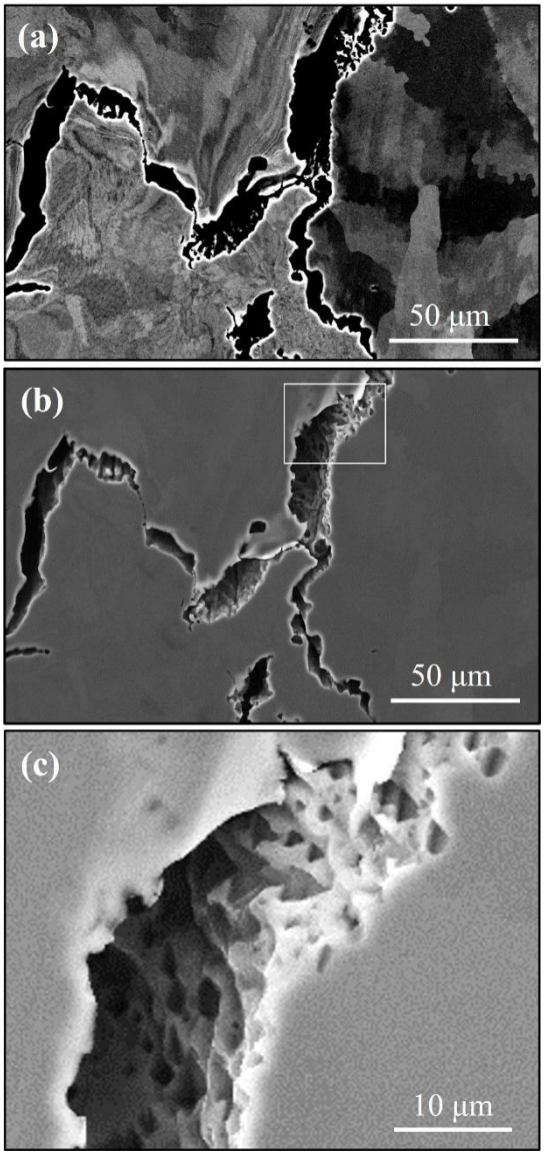

Fig. 6. (a) BSE and (b) SE micrographs of a cracked region of the V_{50} specimen. (c) A magnified view of the rectangular region in (b).

3.2.3. Solidification cracking susceptibility vs. thermal stress

It should be noted that each alloy has intrinsic susceptibility to solidification cracking to a certain extent. Furthermore, the presence of high enough thermal stresses is an external condition. The combination of these two factors is necessary conditions for solidification cracking. The solidification cracking susceptibility can be evaluated by a material constant, i.e. the critical temperature range $\Delta T_{\mathrm{CRT}} = T\ (f_s = 0.95) - T\ (f_s = 1)$. As proposed in Ref. [65], this critical temperature range determines the total strain ε at the very last stage of solidification, according to $\varepsilon = \alpha \cdot \Delta T_{CRT} + 0.05 \cdot \beta^{1/3}$, where α is the thermal expansion coefficient of the alloy and β is volume shrinkage coefficient of the liquid during solidification. Obviously, this equation indicates that a larger ΔT_{CRT} value results in a larger total strain ε occurred at the very last stage of solidification. When the strain cannot be accommodated by the elastic and plastic deformation of the alloy, solidification cracking occurs. According to our Scheil solidification simulation result which will be presented later in Fig. 8, the CrCoNi MPEA solidifies in a very narrow ΔT_{CRT} range of 16 K that is much smaller than 350 K of some non-weldable Ni-

based superalloys [65] and comparable to that of weldable 316L stainless steels [36]. Therefore, the CrCoNi alloy can be classified as a "weldable/printable" alloy system in terms of its low susceptibility to solidification cracking, and this could also be observed from the good quality of our cracks-free V_{10} specimen.

However, we detected severe solidification cracking in the V_{50} specimen. Similarly, Bi et al. also observed severe hot cracking in the DED-processed CrCoNi specimen, which is related to the oxidation mechanism (reaching up to ~ 550 ppm) and corresponding weakened plastic deformation capability [16]. However, the oxygen content of our CrCoNi pre-alloyed powders prepared by plasma rotating electrode process was measured to be as low as ~ 80 ppm. And the DED process was performed in an ultra-high-purity argon-filled atmosphere with oxygen levels below 10 ppm. This restricts the oxygen levels of final DED-processed CrCoNi specimens in our study below 120 ppm, which make us safely exclude the oxidation mechanisms. As for the severe solidification cracking in the V_{50} specimen, the reasons have been directed towards the external reason, i.e., the high thermal stress. Indirect evidence for the considerable thermal stress can be observed from the typical ECCI images in Fig. 7. The V_{10} specimen contains discrete dislocations (Fig. 7 a), and in contrast, the dislocations in the V_{50} specimen are much denser (Fig. 7 b). Two slip traces are clearly shown, forming an angle of 60 degrees. Furthermore, the stacking faults are frequently observed in the V_{50} specimen, as marked by the white arrows in Fig. 7 b. Such a high density of crystallographic defects (both dislocations and stacking faults) suggest the presence of higher residual stresses in the V_{50} specimen as compared with the V_{10} specimen. Hence, severe solidification cracking is activated in the V_{50} specimen despite of low solidification cracking susceptibility.

It naturally follows to discuss the origin of the high thermal stress in the V_{50} specimen. The considerable thermal stress may originate from the extremely coarse columnar grains [36]. For example, similar to our CrCoNi alloy, the CoCrFeNi MPEA also exhibits a very narrow ΔT_{CRT} range but shows severe solidification cracking. As revealed by Sun et al. [36], the extremely large columnar grains (~ 200 μm in width and ~ 3 mm in length) are the origin of the considerable thermal stress and hence the intergranular solidification cracking of the AM-processed CoCrFeNi MPEA. Such grain size effects on the intergranular solidification cracking were also reported in other "weldable/printable" conventional alloys [66]. However, the grain size effects are not believed to be the origin of the high thermal stress and intergranular solidification cracking of our V_{50} specimen. This is because the V_{50} specimen has a grain structure of columnar plus equiaxed, with a smaller grain size, compared with the V_{10} specimen that is free of any cracks. In this study, we attributed the high thermal stress and hence the severe solidification cracking of our V_{50} specimen to the high laser scan speed and corresponding high temperature gradient. As we all know, the DED process is characterized by deposition and solidification of successive layers. The cooling of depositing layers would be restricted by the cooler substrate and prior deposited layers, which would create a tensile stress in the depositing layers [67, 68]. The increased laser scan speed inevitably aggravates the rapid cooling of the melt pool and gives rise to the substantial temperature gradients, as shown in Fig. 3. As a direct result, the thermal stress in the V_{50} specimen would be amplified as compared with the V_{10} specimen. The high thermal stress could pull up the liquid film wetting the dendrites at the last stage of solidification. Furthermore, it's worth mentioning that the hot cracks in the V_{50} specimen preferably develop in the regions of columnar grains instead of the regions of fine equiaxed grains. This may be due to the fact that the fine equiaxed-grained regions

could more easily accommodate the high thermal stress and strain [69].

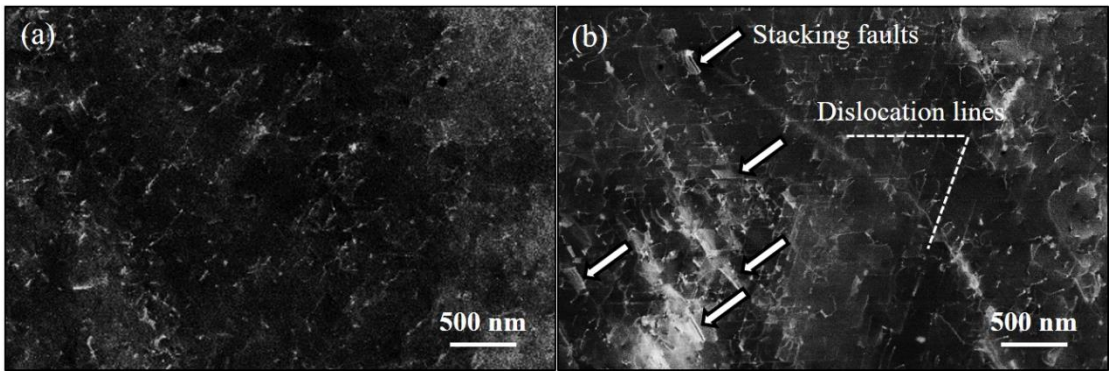

Fig. 7. ECCI images of the (a) V_{10} and (b) V_{50} specimens taken on the uncracked regions, showing the crystallographic defects. Stacking faults and denser dislocations were observed in the V_{50} specimen. Two slip traces are formed with an angle of 60 degrees, as indicated by the broken white lines in b. The stacking faults are also indicated by the arrows in b.

3.3. Phase and microstructure formation

3.3.1. Phase formation

The XRD patterns in Fig. 8 suggest that the DED-processed CrCoNi specimens exhibit a single-phase FCC structure, regardless of the laser scan speed. This is in good agreement with their counterparts processed by conventional routes [53]. Such a simple single-phase structure can be discussed with the aid of the thermodynamic calculations (Fig. 9). Under the assumption of the infinite diffusion of all the elements in both solids and liquids (i.e. equilibrium solidification), we predicted that only FCC phase solidifies from the melt, i.e. L → L + FCC → FCC. The Scheil-Gulliver solidification was also performed based on the assumption of the infinite diffusion of all the elements in the liquid and no diffusion of all the elements in the solid. Clearly, the Scheil-Gulliver solidification has a similar solidification path, also leading to the formation of a single-phase FCC structure. For the Scheil-Gulliver case, however, it is clear that the effect of micro-segregation is considered but overestimated and hence predicts a much lower solidus temperature, i.e., 1678 K for Scheil-Gulliver solidification versus 1707 K for equilibrium solidification.

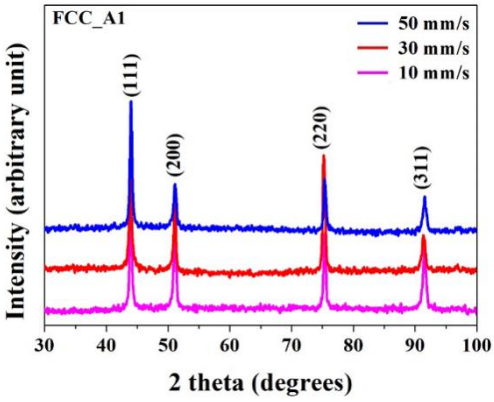

Fig. 8. XRD patterns of the DED-processed CrCoNi specimens deposited at various

laser scan speeds, showing a single-phase FCC structure.

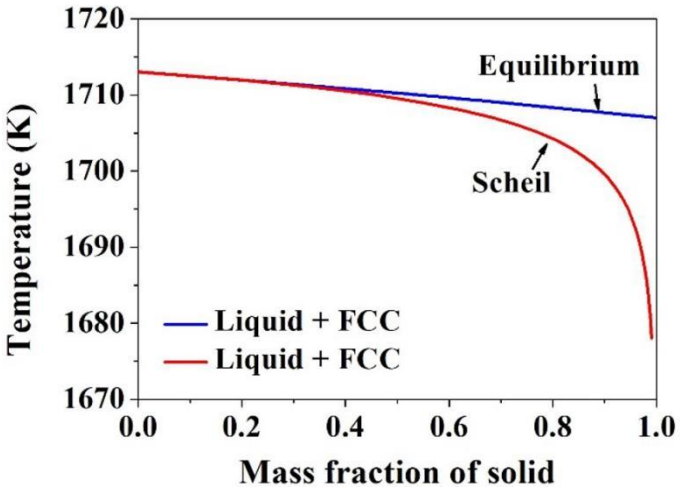

Fig. 9. Thermodynamic prediction of the solidification path of the CrCoNi alloy based on both equilibrium and Scheil-Gulliver assumptions.

3.3.2. Grain growth and cellular substructures

In the following sections, we used V_{10} and V_{50} specimens to study the grain structure formation. Fig. 10 presents the EBSD IPF, image quality (IQ) and KAM maps of the V_{10} and V_{50} specimens with a scan area of 1 × 1 mm^2. The examination surface is the YZ-plane, with Y-axis aligned horizontally and Z-axis aligned vertically. In the IPF and IQ maps, the HAGBs and LAGBs are highlighted in black and in blue, respectively. For the KAM maps, only HAGBs (in black) are highlighted. It can be observed from the IPF map in Fig. 10 a that the grain structure, delineated by HAGBs, is overall columnar in the front view of the V_{10} specimen. The longitudinal axes of these elongated grains deviate from the build direction and are along various directions. Furthermore, the longitudinal axes of some elongated grains rotate by 90° at certain locations. The growth of these elongated grains can be well discussed in terms of the melt pool boundaries. The melt pool boundaries are superimposed by the black broken lines in the IQ map (Fig. 10 b). It can be clearly seen from the IQ map that these elongated grains grow across the melt pool boundaries, suggesting the epitaxial growth mode. Furthermore, the longitudinal axes are approximately perpendicular to the local melt pool boundaries, i.e. approximately along the maximum heat flux direction. The 90° rotation of the longitudinal axes occurs only when the grains run across the melt pool boundaries. A typical columnar grain that rotates by 90° is marked by red arrows in Fig. 10 b. In contrast to the V_{10} specimen, the V_{50} specimen has a much more heterogenous grain structure. Both columnar and equiaxed grains were observed in the front view (Fig. 10 d and e). Elongated and equiaxed grains are formed alternately, as marked in Fig. 10 e. These elongated grains form a convergent pattern (i.e. towards a centerline). In the adjacent column, the grains are much more equiaxed.

Furthermore, it should be noted that the grains in the IPF maps are colored based on their orientations with respect to the build direction (Fig. 10 a and d). A continuous color change and thus a local misorientation were frequently observed within individual

grains, especially across the LAGBs (subgrain boundaries). The local misorientation is directly evidenced in the KAM maps, as shown in Fig. 10 c and f. By comparing the IPF and KAM maps, a more direct correlation between the misorientation and the LAGBs is confirmed. More specifically, the formation of the LAGBs introduces a large local misorientation. This is reasonable because the subgrains grow together to form a single grain by the introduction of a LAGB. Such a growth process will lead to a larger misorientation at LAGBs than other regions within individual grains. In this study, the total length of the LAGBs in the V_{10} and V_{50} specimens was measured to be ~ 15 and 33 mm, respectively, in an equal investigated area of 1 × 1 mm^2. The denser LAGBs in the V_{50} specimen inevitably leads to a more frequent local misorientation, as compared to the V_{10} specimen (Fig. 10 c and f).

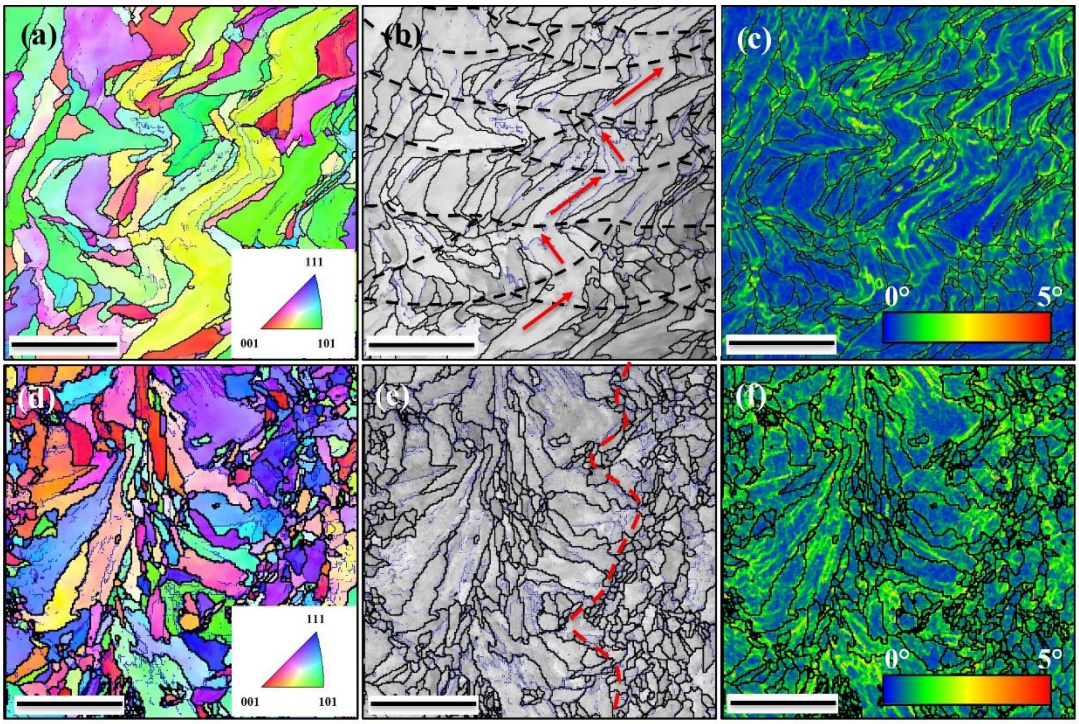

Fig. 10. EBSD characterization of the (a) – (c) V_{10} and (d) – (f) V_{50} specimens (front view). (a) and (d) are IPF maps, (b) and (e) are IQ maps, and (c) and (f) are KAM maps. In the IPF and IQ maps, the HAGBs and LAGBs are highlighted in black and in blue, respectively. In the KAM maps, only the HAGBs are highlighted. The black dashed lines in (b) represent the melt pool boundaries. A typical columnar grain that rotates 90° is marked by red arrows in (b). The red dashed line in (e) delineate alternate regions of columnar and equiaxed morphologies in the V_{50} specimen. The reference axis for the IPF maps is the Z-axis that is aligned vertically upwards. All the scale bars are 300 μm.

To study the intragrain microstructural features, the V_{10} and V_{50} specimens were electrolytically etched and then examined by OM and SEM, and the results are shown in Figs. 11-12. First, we observed similar grain structures in both samples, as revealed by EBSD in Fig. 10, i.e., typically columnar grains in the V_{10} specimen and columnar plus equiaxed grains in the V_{50} specimen. Furthermore, we observed typical cellular substructures in the V_{10} and V_{50} specimens, without obvious dendritic structures. The elimination of the dendritic structures is attributed to the high cooling rates during the

melt pool solidification, as evidenced by Fig. 3, which enable to suppress the formation of the secondary arms. As compared with the V_{10} specimen, the V_{50} specimen shows a finer cellular substructure. In other words, the cellular spacing decreases with the increase of the laser scan speed, as summarized in Fig. 13 a. Such a tendency is attributed to the variation in the cooling rate, and the relationship between the cellular spacing and the cooling rate is established, as shown in Fig. 13 b. Many conventional alloys (e.g. steels) also show a similar trend during the AM processes [70, 71], and by fitting the experimental data in this study, a new equation describing the quantitative relationship between the cellular spacing and the cooling rate is proposed for the CrCoNi MPEA system as follows:

$$\lambda = 8.81 \cdot (CR)^{-0.13}$$

where λ is the cellular spacing in μm, and CR is the cooling rate in K/s.

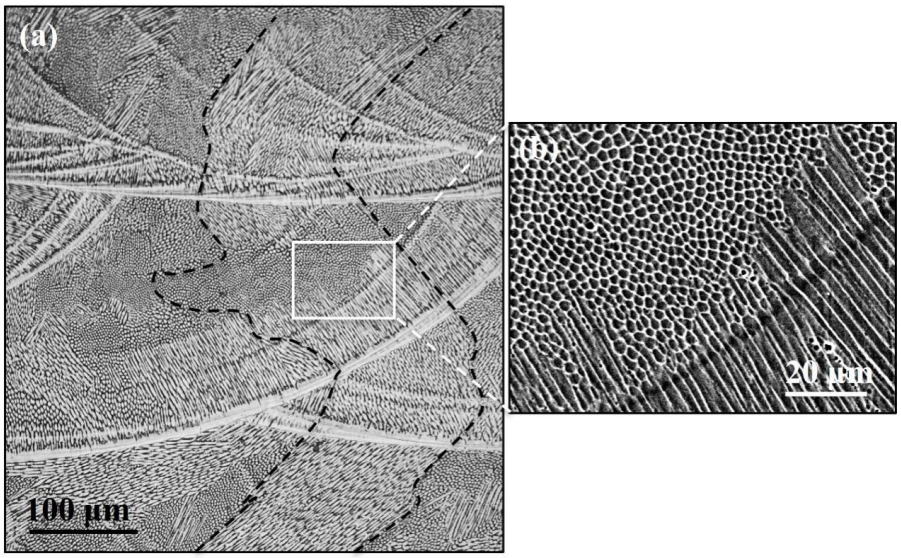

Fig. 11. (a) OM and (b) SEM micrographs of the V_{10} specimen, showing the columnar grains and internal cellular substructures.

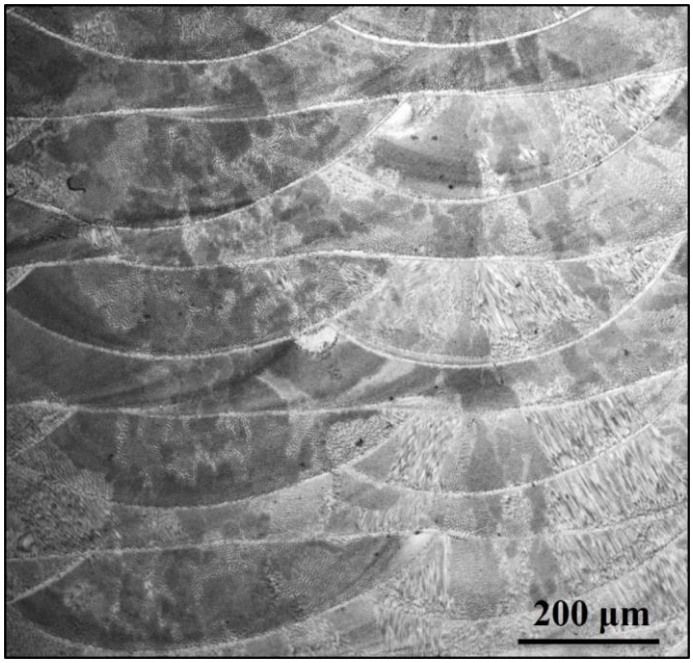

Fig. 12. A typical OM micrograph of the V_{50} specimen, showing the alternate columnar and equiaxed grains.

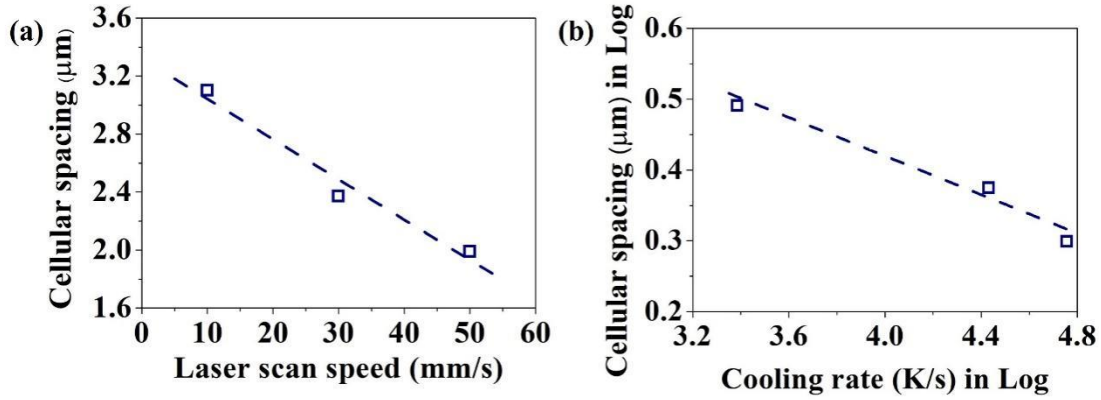

Fig. 13. Effects of (a) the laser scan speed and (b) the cooling rate on the cellular substructure size.

4. Conclusions

In this study, we additively manufactured CrCoNi by DED at different laser scan speeds of 10, 30, and 50 mm/s, and special focus was given to the thermal behavior, cracking behavior and microstructure formation. The main conclusions emerging from the present work are:

(i) The increase in the laser scan speed from 10 to 50 mm/s causes a simultaneous increase in temperature gradients and cooling rates, as measured by a high-speed and high-resolution thermal pyrometer. The temperature gradient and cooling rate for the specimen deposited at a laser scan speed of 50 mm/s reach as high as 1,148 K/mm and 57,778 K/s, respectively.

(ii) Severe cracking has been observed in the sample deposited at a laser scan speed of 50 mm/s. As revealed by EBSD, these cracks propagate along high angle grain

boundaries. Further microstructural characterization reveals the protruding dendrites from the cracked plane. Altogether, these cracks are classified as solidification cracking.

(iii) The Scheil-Gulliver solidification predicts a very narrow critical temperature range of 16 K which is indicative of a low solidification cracking susceptibility. The severe solidification cracking of the CrCoNi MPEA deposited at a laser scan speed of 50 mm/s is attributed to the high temperature gradient and the resulting high residual stress.

(iv) With increasing the laser scan speed from 10 to 50 mm/s, the grain structure changes from elongated grains, which are roughly oriented along the build direction, to a more heterogenous grain structure with elongated grains converging towards the centerline and equiaxed grains arranged between the columns of elongated grains. Furthermore, the increased laser scan speed refines the cell structures due to the increased cooling rates. Dislocations and stacking faults are also activated in the sample deposited at high laser scan speeds due to the high thermal stress.

Declaration of Competing Interest

The authors declare that they have no known competing financial interests or personal relationships that could have appeared to influence the work reported in this paper.

Acknowledgements

The work described in this paper was mainly supported by the funding support to the State Key Laboratories in Hong Kong from the Innovation and Technology Commission (ITC) of the Government of the Hong Kong Special Administrative Region (HKSAE), China. The authors would also like to express their sincere thanks to the financial support from the Research Committee (Project code: BBXD and BBX2) of The Hong Kong Polytechnic University.

References

[1] B. Cantor, I.T.H. Chang, P. Knight, A.J.B. Vincent, Microstructural development in equiatomic multicomponent alloys, Mater. Sci. Eng. A 375-377 (2004) 213-218.
[2] O.N. Senkov, J.D. Miller, D.B. Miracle, C. Woodward, Accelerated exploration of multi-principal element alloys with solid solution phases, Nat. Commun. 6 (2015) 1-10.
[3] B. Gludovatz, A. Hohenwarter, D. Catoor, E.H. Chang, E.P. George, R.O. Ritchie, A fracture-resistant high-entropy alloy for cryogenic applications, Science 345(6201) (2014) 1153-8.
[4] P.J. Shi, W.L. Ren, T.X. Zheng, Z.M. Ren, X.L. Hou, J.C. Peng, P.F. Hu, Y.F. Gao, Y.B. Zhong, P.K. Liaw, Enhanced strength-ductility synergy in ultrafine-grained eutectic high-entropy alloys by inheriting microstructural lamellae, Nat. Commun. 10 (2019).
[5] A. Takeuchi, K. Amiya, T. Wada, K. Yubuta, W. Zhang, High-entropy alloys with a hexagonal close-packed structure designed by equi-atomic alloy strategy and binary phase diagrams, JOM 66(10) (2014) 1984-1992.
[6] M.C. Gao, B. Zhang, S.M. Guo, J.W. Qiao, J.A. Hawk, High-entropy alloys in hexagonal close-packed structure, Metall. Mater. Trans. A 47(7) (2016) 3322-3332.

[7] Y.-J. Liang, L. Wang, Y. Wen, B. Cheng, Q. Wu, T. Cao, Q. Xiao, Y. Xue, G. Sha, Y. Wang, Y. Ren, X. Li, L. Wang, F. Wang, H. Cai, High-content ductile coherent nanoprecipitates achieve ultrastrong high-entropy alloys, Nat. Commun. 9(1) (2018) 4063.
[8] B. Gludovatz, A. Hohenwarter, K.V. Thurston, H. Bei, Z. Wu, E.P. George, R.O. Ritchie, Exceptional damage-tolerance of a medium-entropy alloy CrCoNi at cryogenic temperatures, Nat Commun 7 (2016) 10602.
[9] B. Gludovatz, A. Hohenwarter, D. Catoor, E.H. Chang, E.P. George, R.O. Ritchie, A fracture-resistant high-entropy alloy for cryogenic applications, Science 345(6201) (2014) 1153-1158.
[10] Z. Tang, T. Yuan, C.-W. Tsai, J.-W. Yeh, C.D. Lundin, P.K. Liaw, Fatigue behavior of a wrought $Al_{0.5}$CoCrCuFeNi two-phase high-entropy alloy, Acta Mater. 99 (2015) 247-258.
[11] Z. Wu, H. Bei, G.M. Pharr, E.P. George, Temperature dependence of the mechanical properties of equiatomic solid solution alloys with face-centered cubic crystal structures, Acta Mater. 81 (2014) 428-441.
[12] Z. Wu, H. Bei, F. Otto, G.M. Pharr, E.P. George, Recovery, recrystallization, grain growth and phase stability of a family of FCC-structured multi-component equiatomic solid solution alloys, Intermetallics 46 (2014) 131-140.
[13] W. Ji, W.M. Wang, H. Wang, J.Y. Zhang, Y.C. Wang, F. Zhang, Z.Y. Fu, Alloying behavior and novel properties of CoCrFeNiMn high-entropy alloy fabricated by mechanical alloying and spark plasma sintering, Intermetallics 56 (2015) 24-27.
[14] Y. Zou, H. Ma, R. Spolenak, Ultrastrong ductile and stable high-entropy alloys at small scales, Nat. Commun. 6 (2015).
[15] Y.M. Wang, T. Voisin, J.T. McKeown, J.C. Ye, N.P. Calta, Z. Li, Z. Zeng, Y. Zhang, W. Chen, T.T. Roehling, R.T. Ott, M.K. Santala, P.J. Depond, M.J. Matthews, A.V. Hamza, T. Zhu, Additively manufactured hierarchical stainless steels with high strength and ductility, Nat. Mater. 17(1) (2018) 63.
[16] X. Bi, R. Li, T. Li, X. Zhang, J. Cheng, Y. Tian, Cracks suppression strategies for CoCrNi medium entropy alloy fabricated by laser directed energy deposition, Mater. Des. 226 (2023) 111579.
[17] M.T. Tran, T.H. Nguyen, D.-K. Kim, W. Woo, S.-H. Choi, H.W. Lee, H. Wang, J.G. Kim, Effect of hot isostatic pressing on the cryogenic mechanical properties of CrCoNi medium entropy alloy processed by direct energy deposition, Mater. Sci. Eng. A 828 (2021) 142110.
[18] C. Pan, X. Li, H. Luo, K. Kosiba, S. Qu, C. Yang, D. Zhu, C. Zhang, Tuning the strength and ductility balance of a Co32Cr36Ni32 medium entropy alloy fabricated by selective laser melting: Effect of segregations along grain boundaries, Mater. Sci. Eng. A 840 (2022) 142923.
[19] J. Wang, J. Zou, H. Yang, Z. Liu, S. Ji, High strength and ductility of an additively manufactured CrCoNi medium-entropy alloy achieved by minor Mo doping, Mater. Sci. Eng. A 843 (2022) 143129.
[20] Z.G. Zhu, Q.B. Nguyen, F.L. Ng, X.H. An, X.Z. Liao, P.K. Liaw, S.M.L. Nai, J. Wei, Hierarchical microstructure and strengthening mechanisms of a CoCrFeNiMn

high entropy alloy additively manufactured by selective laser melting, Scr. Mater. 154 (2018) 20-24.
[21] R.D. Li, P.D. Niu, T.C. Yuan, P. Cao, C. Chen, K.C. Zhou, Selective laser melting of an equiatomic CoCrFeMnNi high-entropy alloy: processability, non-equilibrium microstructure and mechanical property, J. Alloys Compd. 746 (2018) 125-134.
[22] A. Piglione, B. Dovgyy, C. Liu, C.M. Gourlay, P.A. Hooper, M.S. Pham, Printability and microstructure of the CoCrFeMnNi high-entropy alloy fabricated by laser powder bed fusion, Mater. Lett. 224 (2018) 22-25.
[23] Z. Qiu, C. Yao, K. Feng, Z. Li, P.K. Chu, Cryogenic deformation mechanism of CrMnFeCoNi high-entropy alloy fabricated by laser additive manufacturing process, Int. J. Lightweight Mater. Manuf. 1(1) (2018) 33-39.
[24] S. Xiang, H.W. Luan, J. Wu, K.F. Yao, J.F. Li, X. Liu, Y.Z. Tian, W.L. Mao, H. Bai, G.M. Le, Q. Li, Microstructures and mechanical properties of CrMnFeCoNi high entropy alloys fabricated using laser metal deposition technique, J. Alloys Compd. 773 (2019) 387-392.
[25] X. Gao, Y. Lu, Laser 3D printing of CoCrFeMnNi high-entropy alloy, Mater. Lett. 236 (2019) 77-80.
[26] Z. Tong, X. Ren, J. Jiao, W. Zhou, Y. Ren, Y. Ye, E.A. Larson, J. Gu, Laser additive manufacturing of FeCrCoMnNi high-entropy alloy: effect of heat treatment on microstructure, residual stress and mechanical property, J. Alloys Compd. 785 (2019) 1144-1159.
[27] S. Guan, D. Wan, K. Solberg, F. Berto, T. Welo, T.M. Yue, K.C. Chan, Additive manufacturing of fine-grained and dislocation-populated CrMnFeCoNi high entropy alloy by laser engineered net shaping, Mater. Sci. Eng. A 761 (2019) 138056.
[28] Y. Chew, G.J. Bi, Z.G. Zhu, F.L. Ng, F. Weng, S.B. Liu, S.M.L. Nai, B.Y. Lee, Microstructure and enhanced strength of laser aided additive manufactured CoCrFeNiMn high entropy alloy, Mater. Sci. Eng. A 744 (2019) 137-144.
[29] M.A. Melia, J.D. Carroll, S.R. Whetten, S.N. Esmaeely, J. Locke, E. White, I. Anderson, M. Chandross, J.R. Michael, N. Argibay, E.J. Schindelholz, A.B. Kustas, Mechanical and corrosion properties of additively manufactured CoCrFeMnNi high entropy alloy, Addit. Manuf. 29 (2019) 100833.
[30] I. Kunce, M. Polanski, K. Karczewski, T. Plocinski, K.J. Kurzydlowski, Microstructural characterisation of high-entropy alloy AlCoCrFeNi fabricated by laser engineered net shaping, J. Alloys Compd. 648 (2015) 751-758.
[31] T. Fujieda, H. Shiratori, K. Kuwabara, T. Kato, K. Yamanaka, Y. Koizumi, A. Chiba, First demonstration of promising selective electron beam melting method for utilizing high-entropy alloys as engineering materials, Mater. Lett. 159 (2015) 12-15.
[32] H. Shiratori, T. Fujieda, K. Yamanaka, Y. Koizumi, K. Kuwabara, T. Kato, A. Chiba, Relationship between the microstructure and mechanical properties of an equiatomic AlCoCrFeNi high-entropy alloy fabricated by selective electron beam melting, Mater. Sci. Eng. A 656 (2016) 39-46.
[33] J. Joseph, P. Hodgson, T. Jarvis, X.H. Wu, N. Stanford, D.M. Fabijanic, Effect of hot isostatic pressing on the microstructure and mechanical properties of additive manufactured Al_xCoCrFeNi high entropy alloys, Mater. Sci. Eng. A 733 (2018) 59-70.

[34] J. Joseph, T. Jarvis, X.H. Wu, N. Stanford, P. Hodgson, D.M. Fabijanic, Comparative study of the microstructures and mechanical properties of direct laser fabricated and arc-melted $Al_xCoCrFeNi$ high entropy alloys, Mater. Sci. Eng. A 633 (2015) 184-193.
[35] J. Joseph, N. Stanford, P. Hodgson, D.M. Fabijanic, Tension/compression asymmetry in additive manufactured face centered cubic high entropy alloy, Scr. Mater. 129 (2017) 30-34.
[36] Z. Sun, X.P. Tan, M. Descoins, D. Mangelinck, S.B. Tor, C.S. Lim, Revealing hot tearing mechanism for an additively manufactured high-entropy alloy via selective laser melting, Scr. Mater. 168 (2019) 129-133.
[37] Y. Brif, M. Thomas, I. Todd, The use of high-entropy alloys in additive manufacturing, Scr. Mater. 99 (2015) 93-96.
[38] R. Zhou, Y. Liu, C.S. Zhou, S.Q. Li, W.Q. Wu, M. Song, B. Liu, X.P. Liang, P.K. Liaw, Microstructures and mechanical properties of C-containing FeCoCrNi high-entropy alloy fabricated by selective laser melting, Intermetallics 94 (2018) 165-171.
[39] D. Choudhuri, T. Alam, T. Borkar, B. Gwalani, A.S. Mantri, S.G. Srinivasan, M.A. Gibson, R. Banerjee, Formation of a Huesler-like L21 phase in a CoCrCuFeNiAlTi high-entropy alloy, Scr. Mater. 100 (2015) 36-39.
[40] I. Kunce, M. Polanski, J. Bystrzycki, Microstructure and hydrogen storage properties of a TiZrNbMoV high entropy alloy synthesized using laser engineered net shaping (LENS), Int. J. Hydrog. Energy 39(18) (2014) 9904-9910.
[41] T. Fujieda, H. Shiratori, K. Kuwabara, M. Hirota, T. Kato, K. Yamanaka, Y. Koizumi, A. Chiba, S. Watanabe, CoCrFeNiTi-based high-entropy alloy with superior tensile strength and corrosion resistance achieved by a combination of additive manufacturing using selective electron beam melting and solution treatment, Mater. Lett. 189 (2017) 148-151.
[42] S. Guan, K. Solberg, D. Wan, F. Berto, T. Welo, T.M. Yue, K.C. Chan, Formation of fully equiaxed grain microstructure in additively manufactured $AlCoCrFeNiTi_{0.5}$ high entropy alloy, Mater. Des. 184 (2019) 108202.
[43] T. Borkar, V. Chaudhary, B. Gwalani, D. Choudhuri, C.V. Mikler, V. Soni, T. Alam, R.V. Ramanujan, R. Banerjee, A combinatorial approach for assessing the magnetic properties of high entropy alloys: role of Cr in $AlCo_xCr_{1-x}FeNi$, Adv. Eng. Mater. 19(8) (2017) 1700048.
[44] T. Borkar, B. Gwalani, D. Choudhuri, C.V. Mikler, C.J. Yannetta, X. Chen, R.V. Ramanujan, M.J. Styles, M.A. Gibson, R. Banerjee, A combinatorial assessment of AlxCrCuFeNi2 ($0 < x < 1.5$) complex concentrated alloys: microstructure, microhardness, and magnetic properties, Acta Mater. 116 (2016) 63-76.
[45] B. Gwalani, V. Soni, O.A. Waseem, S.A. Mantri, R. Banerjee, Laser additive manufacturing of compositionally graded AlCrFeMoVx ($x = 0$ to 1) high-entropy alloy system, Opt. Laser Technol. 113 (2019) 330-337.
[46] S. Guan, D. Wan, K. Solberg, F. Berto, T. Welo, T.M. Yue, K.C. Chan, Additively manufactured $CrMnFeCoNi/AlCoCrFeNiTi_{0.5}$ laminated high-entropy alloy with enhanced strength-plasticity synergy, Scr. Mater. 183 (2020) 133-138.
[47] Y. Chen, F.G. Lu, K. Zhang, P.L. Nie, S.R.E. Hosseini, K. Feng, Z.G. Li, Dendritic

microstructure and hot cracking of laser additive manufactured Inconel 718 under improved base cooling, J. Alloys Compd. 670 (2016) 312-321.
[48] Y. Chen, F.G. Lu, K. Zhang, P.L. Nie, S.R.E. Hosseini, K. Feng, Z.G. Li, P.K. Chu, Investigation of dendritic growth and liquation cracking in laser melting deposited Inconel 718 at different laser input angles, Mater. Des. 105 (2016) 133-141.
[49] Y. Chen, K. Zhang, J. Huang, S.R.E. Hosseini, Z.G. Li, Characterization of heat affected zone liquation cracking in laser additive manufacturing of Inconel 718, Mater. Des. 90 (2016) 586-594.
[50] O.A. Ojo, N.L. Richards, M.C. Chaturvedi, Contribution of constitutional liquation of gamma prime precipitate to weld HAZ cracking of cast Inconel 738 superalloy, Scr. Mater. 50(5) (2004) 641-646.
[51] S. Asavavisithchai, W. Homkrajai, P. Wangyao, Strain-age cracking after postweld heat treatments in Inconel 738 superalloy, High Temp. Mater. Processes (London), 2010, p. 61.
[52] A.J. Ramirez, J.C. Lippold, High temperature behavior of Ni-base weld metal: part II. insight into the mechanism for ductility dip cracking, Mater. Sci. Eng. A 380(1) (2004) 245-258.
[53] B. Gludovatz, A. Hohenwarter, K.V.S. Thurston, H. Bei, Z. Wu, E.P. George, R.O. Ritchie, Exceptional damage-tolerance of a medium-entropy alloy CrCoNi at cryogenic temperatures, Nat. Commun. 7 (2016).
[54] R. Cunningham, A. Nicolas, J. Madsen, E. Fodran, E. Anagnostou, M.D. Sangid, A.D. Rollett, Analyzing the effects of powder and post-processing on porosity and properties of electron beam melted Ti-6Al-4V, Mater. Res. Lett. 5(7) (2017) 516-525.
[55] S. Guan, D. Wan, K. Solberg, F. Berto, T. Welo, T.M. Yue, K.C. Chan, Additive manufacturing of fine-grained and dislocation-populated CrMnFeCoNi high entropy alloy by laser engineered net shaping, Mater. Sci. Eng. A 761 (2019).
[56] K.G. Prashanth, S. Scudino, T. Maity, J. Das, J. Eckert, Is the energy density a reliable parameter for materials synthesis by selective laser melting?, Mater. Res. Lett. 5(6) (2017) 386-390.
[57] N.T. Aboulkhair, N.M. Everitt, I. Ashcroft, C. Tuck, Reducing porosity in AlSi10Mg parts processed by selective laser melting, Addit. Manuf. 1-4 (2014) 77-86.
[58] W.E. King, H.D. Barth, V.M. Castillo, G.F. Gallegos, J.W. Gibbs, D.E. Hahn, C. Kamath, A.M. Rubenchik, Observation of keyhole-mode laser melting in laser powder-bed fusion additive manufacturing, J. Mater. Process. Technol. 214(12) (2014) 2915-2925.
[59] H. Peng, Y. Shi, S. Gong, H. Guo, B. Chen, Microstructure, mechanical properties and cracking behaviour in γ'–precipitation strengthened nickel-base superalloy fabricated by electron beam melting, Mater. Des. 159 (2018) 155-169.
[60] Q.Q. Han, R. Mertens, M.L. Montero-Sistiaga, S.F. Yang, R. Setchi, K. Vanmeensel, B. Van Hooreweder, S.L. Evans, H.Y. Fan, Laser powder bed fusion of Hastelloy X: effects of hot isostatic pressing and the hot cracking mechanism, Mater. Sci. Eng. A 732 (2018) 228-239.
[61] O.A. Ojo, N.L. Richards, M.C. Chaturvedi, Study of the fusion zone and heat-affected zone microstructures in tungsten inert gas-welded INCONEL 738LC

superalloy, Metall. Mater. Trans. A 37A(2) (2006) 421-433.
[62] M. Zhong, H. Sun, W. Liu, X. Zhu, J. He, Boundary liquation and interface cracking characterization in laser deposition of Inconel 738 on directionally solidified Ni-based superalloy, Scr. Mater. 53(2) (2005) 159-164.
[63] A.A.N. Németh, D.J. Crudden, D.E.J. Armstrong, D.M. Collins, K. Li, A.J. Wilkinson, C.R.M. Grovenor, R.C. Reed, Environmentally-assisted grain boundary attack as a mechanism of embrittlement in a nickel-based superalloy, Acta Mater. 126 (2017) 361-371.
[64] L. Carter, M. Attallah, R. C. Reed, Laser powder bed fabrication of nickel-base superalloys: influence of parameters; characterisation, quantification and mitigation of cracking, 2012, pp. 577-586.
[65] J. Zhang, R.F. Singer, Hot tearing of nickel-based superalloys during directional solidification, Acta Mater. 50(7) (2002) 1869-1879.
[66] H. Yamamoto, S. Harada, T. Ueyama, S. Ogawa, F. Matsuda, K. Nakata, Beneficial effects of low- frequency pulsed MIG welding on grain refinement of weld metal and improvement of solidification crack susceptibility of aluminium alloys: study of low-frequency pulsed MIG welding, Weld. Int. 7(6) (1993) 456-461.
[67] W. Chen, T. Voisin, Y. Zhang, J.B. Forien, C.M. Spadaccini, D.L. McDowell, T. Zhu, Y.M. Wang, Microscale residual stresses in additively manufactured stainless steel, Nat Commun 10(1) (2019) 4338.
[68] T. DebRoy, H.L. Wei, J.S. Zuback, T. Mukherjee, J.W. Elmer, J.O. Milewski, A.M. Beese, A. Wilson-Heid, A. De, W. Zhang, Additive manufacturing of metallic components – Process, structure and properties, Prog. Mater. Sci. 92 (2018) 112-224.
[69] J.H. Martin, B.D. Yahata, J.M. Hundley, J.A. Mayer, T.A. Schaedler, T.M. Pollock, 3D printing of high-strength aluminium alloys, Nature 549(7672) (2017) 365-369.
[70] B. Zheng, Y. Zhou, J.E. Smugeresky, J.M. Schoenung, E.J. Lavernia, Thermal behavior and microstructure evolution during laser deposition with laser-engineered net shaping: part II. experimental investigation and discussion, Metall. Mater. Trans. A 39A(9) (2008) 2237-2245.
[71] H. Yin, S.D. Felicelli, Dendrite growth simulation during solidification in the LENS process, Acta Mater. 58(4) (2010) 1455-1465.

Declaration of Competing Interest

The authors declare that they have no known competing financial interests or personal relationships that could have appeared to influence the work reported in this paper.